

Image Reconstruction From the Compton Scattering of X-Ray Fan Beams in Thick/Dense Objects

Paul J. Arsenault and Esam M. A. Hussein

Abstract—Image reconstruction from Compton scattering measurements results in a nonlinear inverse problem that can produce multiple solutions, particularly in deep/dense objects. In this work, the nonlinearity of the problem is mitigated by a transformation which minimizes the difference of the ratios of measurements with overlapping fields of view. Overlapping eliminates one of the competing factors in the nonlinear problem, and allows solving the inverse problem of image reconstruction beyond the one-mean-free path equivalent depth previously needed to reach a solution in scatter-only imaging. The method also enables the use of wide X-ray fan beam sources, and is numerically applied to exploit the ability of scatter imaging to acquire single-side two-dimensional (2-D) and three-dimensional (3-D) images of relatively dense objects. Examples are presented to demonstrate the method's ability to deal with noisy measurements, at various degrees of overdetermination.

Index Terms—Compton scatter imaging, image reconstruction, X-ray applications.

I. INTRODUCTION

IMAGING using scattered radiation resembles the natural process of optical viewing with the naked eye. Unlike natural vision which sees light reflected off surfaces, scatter imaging by penetrating radiation (X-rays and gamma rays and neutrons) records events that take place deep within a material. The scattering signal is modulated by the attenuation of radiation as it travels toward the point of scattering and then returns to the detection (viewing) point. This makes image reconstruction a nonlinear inverse problem, since the attenuation process is exponential in nature, while the scattering process is linear. The challenge posed by this nonlinearity is best demonstrated by considering the forward problem of modeling the detector response to scattering from a single voxel. We will consider here for simplification the Compton scattering of a pencil beam of monoenergetic photons from a source, i , of some incident energy, \vec{E} , scattered by some angle within an object lumped into a single voxel, j , and returned to a detector k with an energy \overleftarrow{E} , as schematically shown in Fig. 1. The detector response, s_{ijk} , can be expressed as

$$s_{ijk} = c_{ijk} \exp\left[-\vec{\mu}_{ijk} \frac{x}{2}\right] \mu_{ijk} \exp\left[-\overleftarrow{\mu}_{jk} \frac{y}{2}\right] \quad (1)$$

Manuscript received July 25, 2005; revised February 22, 2006. The work of E. M. A. Hussein was supported in part by the Natural Sciences and Engineering Research Council of Canada through a Discovery Grant.

The authors are with the Laboratory for Threat Material Detection, Department of Mechanical Engineering, University of New Brunswick, Fredericton, NB E3B 5A3, Canada (e-mail: LTMD@unb.ca).

Digital Object Identifier 10.1109/TNS.2006.874074

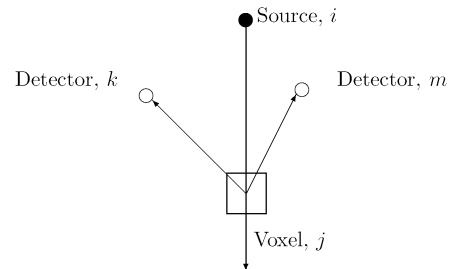


Fig. 1. Schematic for scattering from a single voxel.

where μ refers to the macroscopic Compton scattering cross section, $\vec{\mu}$ and $\overleftarrow{\mu}$ are, respectively, the attenuation coefficients of the incident (incoming) and scattered (outgoing) radiation, x is the distance traveled by the incident radiation within the voxel along the direction of the incident beam, y is the distance along the scattered beam, and c is a predetermined (from calibration measurements) system constant that depends on the voxel's volume, the probability of scattering, source-voxel-detector geometric arrangement, source intensity, detector efficiency, geometry, etc. Note that the model of (1) accounts for all radiation interactions, since $\vec{\mu}$ and $\overleftarrow{\mu}$ are total attenuation coefficients. However, this a model for once-scattered photons, i.e., it does not account for multiple scattering; detector collimation is assumed to facilitate the detection of only single scattering. Compton scattering needs to be the prevalent mode of interaction, in order to obtain strong indications that are not suppressed by photon absorption. The Compton scattering cross section, μ , is proportional to the electron density, hence mass density, for most materials.

To further simplify the problem, we let $x = y$, and replace $\vec{\mu}_{ij}$, μ_{ijk} and $\overleftarrow{\mu}_{jk}$ with some average value, $\bar{\mu}_{ijk}$. Then

$$s_{ijk} = c_{ijk} \bar{\mu}_{ijk} \exp[-\bar{\mu}_{ijk} x]. \quad (2)$$

Equation (2) represents the forward problem that relates a physical parameter, the average attenuation coefficient, to a measurable detector response.

The forward model of (2) demonstrates clearly the competition between the linear term (scattering), which increases with increasing $\bar{\mu}$ and the exponential term (attenuation) that declines in value with increasing $\bar{\mu}$; with the subscripts being dropped for brevity. Therefore, s increases with $\bar{\mu}$ until it reaches a maximum value at $\bar{\mu} = x^{-1}$, then it decreases with increasing $\bar{\mu}$. Note that negative values for $\bar{\mu}$ and s are never considered since such situation has no physical basis. Upon solving the inverse

problem to find the value for $\bar{\mu}$ at a given value s , two solutions are possible. The first solution is for $\bar{\mu} < x^{-1}$ and the other solution at $\bar{\mu} > x^{-1}$. A single solution only exists at $\bar{\mu}x = 1$, where s reaches its maximum value, at which point $x = (1/\bar{\mu})$, i.e., equal to one mean-free-path (mfp). Clearly, the linear component is dominant when $\bar{\mu}x < 1$, while the exponential component is dominant when $\bar{\mu}x > 1$. An iterative solution of (1) can converge to either one of the two possible solutions. When dealing with more than one voxel to reconstruct a realistic image, oscillation between the two possible values of $\bar{\mu}$ at each voxel can result in an unstable iterative process. Previous workers overcame this problem by restricting the solution to objects with a thickness less than one mfp of the radiation used.

When the scatter imaging technique was first introduced by Lale [1], attenuation was completely neglected, rendering a linear problem. In further work by Farmer and Collins [2], the effect of attenuation was partially compensated for using estimates based on the depth of the voxel along the incident beam. Battista and Bronskill [3] determined the attenuation coefficient in each voxel, by sequentially monitoring the scattering from one voxel at a time. Global and simultaneous accounting of the attenuation process was achieved using iterative successive approximations [4], by Hussein and co-workers in neutron-scatter imaging [5] and in imaging with gamma-ray sources [6]. The solutions of [5] and [6] were, however, restricted to thin or light objects to avoid duplicity of solutions.

Solutions for thicker and/or denser objects involved independent *a priori* determination for the attenuation factors, hence the exponential terms. This linearizes the forward problem of (1), and enables direct solution for the density at each voxel. For this purpose, Prettyman *et al.* [7] and Busono and Hussein [8] used independent radiation-transmission tomographic reconstruction; a tedious process that requires multiple exposures to radiation at many directions. More recently, El Khettabi *et al.* [9], [10] avoided full tomographic reconstruction, by utilizing the ratio between two scattering detectors, that share the same incident beam direction and scattering point, as evident from Fig. 1. This ratio in effect reduced the problem to the linear solution of the attenuation coefficient of the scattered radiation, $\bar{\mu}$, but the method is well-suited only to incident pencil beams of radiation. When a wider fan beam is utilized, the ratio between the response of two detectors becomes too convoluted to enable a direct solution for $\bar{\mu}$, even if the two detectors share the same path of incident radiation. This convolution can be unscrambled into equivalent pencil beams for wide mono-directional mono-energetic beams, by measuring the energy spectrum of the scattered radiation, and making use of the unique energy-angle relationship of neutron elastic scattering [5], or photon Compton scattering [6]. For fan and cone beams, as well as for multienergetic radiation, as in the case of X-rays, direct deconvolution of direction by energy is not easily achieved. Since X-ray sources are widely used, and fan, and by extension cone, beams are readily extractable due to the diverging nature of radiation, we have decided to focus on solving the inverse problem of fan X-ray beams. To our knowledge, no previous solution has been obtained for this single-side imaging problem in thick objects with X-ray fan beams.

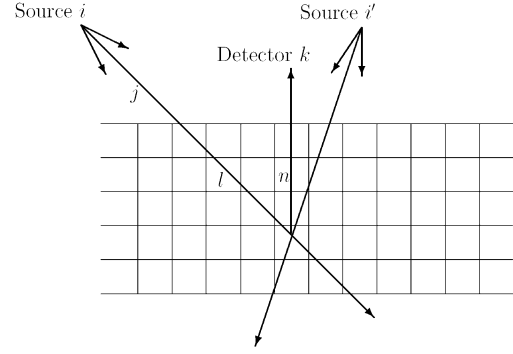


Fig. 2. Schematic showing the passage of two fan beams contributing, one at a time, to a collimated detector. In modeling, each source, i or i' , is divided into elementary beams (j 's), l refers to a voxel in the path of the incoming radiation and n to the voxel scattered radiation encounters in its way to detector k .

II. SOLUTION STRATEGY AND ANALYSIS

A. Forward Problem

An inverse problem cannot be solved without the establishment of the forward problem that maps given theoretical parameters to measurable quantities. The theoretical parameters here are the attenuation coefficients array vectors: $\vec{\mu}$ and $\overleftarrow{\mu}$, and the scattering cross section vector, $\boldsymbol{\mu}$. The measurable quantities are the detector responses, represented by the vector \boldsymbol{S} . The response for a detector k to a source i is simply the summation of the contribution of all individual voxels in the field-of-view of the detector, as given by (1)

$$S_{ik} = \sum_{j=1}^J c_{ijk} \exp \left[- \sum_{l=1}^{L_{ijk}} \vec{\mu}_{ijl} x_{ijl} \right] \times \mu_{ijk} \exp \left[- \sum_{n=1}^{N_{ijk}} \overleftarrow{\mu}_{kn} y_{kn} \right] \quad (3)$$

where the variables are defined as in (1) and the indices, as shown in Fig. 2, define a voxel location along the field of view of a source's elementary beam (a ray) or a detector's field of view, the summation is over J elementary beams for source i , where elementary beam j encounters L_{ijk} voxels before it scatters towards detector k , and N_{ijk} is the number of voxels seen by the detector for elementary beam j of source i . This model has some inherent physical assumptions that were discussed elsewhere [8]; mainly it uses attenuation coefficient values that are the average of those at the incident and scattering energies, and ignores multiple scattering. Verification of the physical validity of this model in a number of practical arrangements is discussed elsewhere [8], [11]. Any discrepancy between this model and the experimental values can be incorporated into the system constants, c_{ijk} 's. When Compton scattering is dominant, it can be assumed that $\vec{\mu}$, $\overleftarrow{\mu}$ and $\boldsymbol{\mu}$ are all proportional to the electron density, and determining one of those parameters leads to the values of the other two. We focus here on solving for $\bar{\mu}$, i.e., the attenuation coefficients at the incident energy. Once the source energy is fixed, the value of $\bar{\mu}$ in the forward model can be determined. In this work, the source energy of a 102 kV X-ray machine was

utilized, as it is one of the common source energies employed in radiography and tomography. At this source energy, $\bar{\mu} \approx 0.2 \text{ cm}^{-1}$ for water at standard temperature and pressure. Changing the source energy does not affect the problem's formulation, except in that it changes the thickness of the imaged material when measured in mfp's ($1 \text{ mfp} = (1/\bar{\mu})$).

B. Inverse Problem

The inverse problem is the mapping of given (or measured) values of detector responses, represented by the vector \mathbf{S} , back to the $\bar{\mu}$ values; where here $\bar{\mu}$ implies reference to the array vectors, $\bar{\mu}$, $\bar{\mu}$, and $\bar{\mu}$, which are interrelated when Compton scattering is dominant. We have attempted in vain a multitude of common methods to solve the inverse problem of reconstructing images from scattered radiation produced by X-ray fan-beams. Iterative successive approximations did not converge due to the competition between the linear and exponential effects. Brute force numerical optimization and various combinations of genetic algorithms did not lead to the correct solution. Various ad-hoc gradient-based methods were attempted, but with little success in the case of dense/thick objects (thickness greater than one mfp). All these methods attempted to match input detector responses with those analytically calculated for a guessed or estimated image configuration. It was clear that the convoluted nature of the fan-beam forward problem, combined with its non-linearity, made it difficult for any solution algorithm to consistently approach a solution. A fundamentally different approach had therefore to be adopted.

C. Strategy

The X-ray scatter imaging problem was recently solved for pencil beams, by taking the ratio between the responses of two detectors that share an overlapping incident beam and a scattering voxel [9]. A fan beam can be viewed as a set of contiguous elementary pencil beams, and the detector response to consist of the sum of the response of individual elementary beams, each given by (1). This summation process and the nonlinear nature of each term inhibits the extraction of common terms that can be cancelled by taking the ratio of detectors that share overlapping fields of view. Nevertheless, such ratio will tend to dampen the effect of the common terms and reduce the competition between the linear and exponential terms. This concept is further expanded here with the view of transforming the inverse problem into a more stable domain.

Conventional least-squares minimization considers the objective function

$$u = \sum_{i=1}^I \sum_{k=1}^K [S_{ik}^* - S_{ik}(\bar{\mu})]^2 \quad (4)$$

where S_{ik}^* is the input (measured) detector response and $S_{ik}(\bar{\mu})$ is the estimated (calculated) detector response for some image with a distribution $\bar{\mu}$, and the summation is over all sources, I , and all detectors K . Note that an individual detector response covers all the voxels exposed by a source and seen by a detector. Therefore, the goal of conventional least-squares minimization

is to find the image $\bar{\mu}$ that minimizes the difference between the recorded measurements and those calculated using the forward model of the problem. Due to the duality of solutions at a given voxel, the objective function of (4) appears to have local optima, preventing convergence to a common global optimum. A modified objective function that compares similar relative independent measurements is therefore proposed. One possible layout is shown in Fig. 2, where two overlapping (complementary) sources having the same incident energy, contributing to the same detector, one at a time, are considered [12]. A collimated detector is employed here to avoid further overlapping of the detected signals. Note that a single source contributing to two complementary detectors could have been used, leading to a similar problem in which a solution is obtained for the distribution of the attenuation coefficient of the scattered radiation. However, by using two sources with a common path to a detector, one can shorten the distance of travel from the scattering voxel to the detector site, and hence reduce the degree of attenuation at the lower photon energy of scattering.

The following objective function is minimized:

$$u_r = \sum_{i=1}^I \sum_{k=1}^K \left[\frac{S_{i'k}}{S_{i'k}^*} - \frac{S_{ik}}{S_{ik}^*} \right]^2 = \sum_{i=1}^I \sum_{k=1}^K R_{i'ik}^2 \quad (5)$$

where now the ratios between estimated measurement (calculated from a guessed image distribution $\bar{\mu}$) and the actual measurement (or that estimated for the actual values of $\bar{\mu}$) for a pair of sources i' and i at a given detector k , or in other words $R_{i'ik}$, is to be minimized.

D. Problem Formulation

In an iterative process, the forward model and its gradient drive the progression from one approximation to another, as evident in the well-known Newton-Raphson method; see for example [13]. The forward model in the objective function of (5) is the function $R_{i'ik}$ expressed, by expanding (1), as

$$\begin{aligned} R_{i'ik} = & \frac{1}{S_{i'k}^*} \sum_{j=1}^J c_{i'jk} \exp \left[- \sum_{l=1}^{L_{i'jk}} \bar{\mu}_{i'jl} x_{i'jl} \right] \\ & \times \mu_{i'jk} \exp \left[- \sum_{n=1}^{N_{i'jk}} \bar{\mu}_{kn} y_{kn} \right] \\ & - \frac{1}{S_{ik}^*} \sum_{j=1}^J c_{ijk} \exp \left[- \sum_{l=1}^{L_{ijk}} \bar{\mu}_{ijl} x_{ijl} \right] \\ & \times \mu_{ijk} \exp \left[- \sum_{n=1}^{N_{ijk}} \bar{\mu}_{kn} y_{kn} \right] \end{aligned} \quad (6)$$

where the same notation as that of (3) is used, with the primed values referring to those of source i' . In order to expose the relative insensitivity of $R_{i'ik}$ to the attenuation coefficients of voxels commonly traversed by sources i' and i , we will simplify (6) by lumping the summations, which cover the effect of many

voxels, into some approximate effective values. This simplifies (6) to

$$R_{i'ik} \approx \tilde{c}_{i'ik} \tilde{\mu}_{i'ik} \exp \left[-\overleftarrow{\tilde{\mu}}_{i'ik} \tilde{Y}_{i'ik} \right] \times \left\{ \frac{1}{S_{i'k}^*} \exp \left[-\overrightarrow{\tilde{\mu}}_{i'k} \tilde{X}_{i'k} \right] - \frac{1}{S_{ik}^*} \exp \left[-\overrightarrow{\tilde{\mu}}_{ik} \tilde{X}_{ik} \right] \right\} \quad (7)$$

where $\tilde{c}_{i'ik}$ is an effective system constant for the assembly of the $i'i$ source pair and detector k , $\tilde{\mu}_{i'ik}$ is an equivalent scattering cross section for the scattering voxels, $\overleftarrow{\tilde{\mu}}_{i'ik}$ is an effective attenuation coefficient for the scattered radiation with $\tilde{Y}_{i'ik}$ being the corresponding distance of travel, and the effective values of $\overrightarrow{\tilde{\mu}}_{i'k}$ and $\overrightarrow{\tilde{\mu}}_{ik}$ are those corresponding to the attenuation coefficients of the radiation incident from source i' and source i before being scattered to detector k , respectively, with $\tilde{X}_{i'k}$ and \tilde{X}_{ik} being respectively equivalent total distances traveled by the radiation from sources i' and i before reaching the center of the scattering volume seen by detector k . In (7), it was assumed that the linear terms in each detector response and the outgoing attenuation terms are approximately equal as they cover the same domain. Now the following partial derivatives of the approximate value of $R_{i'ik}$ can be written

$$\frac{\partial R_{i'ik}}{\partial \overleftarrow{\tilde{\mu}}_{i'ik}} = \tilde{c}_{i'ik} \exp \left[-\overleftarrow{\tilde{\mu}}_{i'ik} \tilde{Y}_{i'ik} \right] \times \left\{ \frac{1}{S_{i'k}^*} \exp \left[-\overrightarrow{\tilde{\mu}}_{i'k} \tilde{X}_{i'k} \right] - \frac{1}{S_{ik}^*} \exp \left[-\overrightarrow{\tilde{\mu}}_{ik} \tilde{X}_{ik} \right] \right\} \quad (8)$$

$$\frac{\partial R_{i'ik}}{\partial \overleftarrow{\tilde{\mu}}_{i'ik}} = -\tilde{c}_{i'ik} \tilde{\mu}_{i'ik} \tilde{Y}_{i'ik} \exp \left[-\overleftarrow{\tilde{\mu}}_{i'ik} \tilde{Y}_{i'ik} \right] \times \left\{ \frac{1}{S_{i'k}^*} \exp \left[-\overrightarrow{\tilde{\mu}}_{i'k} \tilde{X}_{i'k} \right] - \frac{1}{S_{ik}^*} \exp \left[-\overrightarrow{\tilde{\mu}}_{ik} \tilde{X}_{ik} \right] \right\} \quad (9)$$

$$\frac{\partial R_{i'ik}}{\partial \overrightarrow{\tilde{\mu}}_{i'k}} = -\tilde{c}_{i'ik} \tilde{\mu}_{i'ik} \tilde{X}_{i'k} \exp \left[-\overleftarrow{\tilde{\mu}}_{i'ik} \tilde{Y}_{i'ik} \right] \times \left\{ \frac{1}{S_{i'k}^*} \exp \left[-\overrightarrow{\tilde{\mu}}_{i'k} \tilde{X}_{i'k} \right] \right\} \quad (10)$$

$$\frac{\partial R_{i'ik}}{\partial \overrightarrow{\tilde{\mu}}_{ik}} = \tilde{c}_{i'ik} \tilde{\mu}_{i'ik} \tilde{X}_{ik} \exp \left[-\overleftarrow{\tilde{\mu}}_{i'ik} \tilde{Y}_{i'ik} \right] \times \left\{ \frac{1}{S_{ik}^*} \exp \left[-\overrightarrow{\tilde{\mu}}_{ik} \tilde{X}_{ik} \right] \right\}. \quad (11)$$

The derivatives of $R_{i'ik}$ with respect to the common terms of the guessed detector responses $S_{i'k}$ and S_{ik} , given by (8) and (9), are balanced by positive and negative exponential components, rather than only by either a negative or a positive exponential component as in the case of the derivatives with respect

to the uncommon terms, (10) and (11). That is, the derivatives of $R_{i'ik}$ are only mildly affected by changes in the attenuation coefficients or scattering cross sections of the common voxels seen by detector k when exposed to radiation from sources i' and i . In other words, in an iterative process, progression from one iteration to another over $R_{i'ik}$ will not be too sensitive to variations in those common voxels. In fact, in a homogeneous medium with symmetrical sources, the derivatives of $R_{i'ik}$ with respect to the μ 's of the common voxels could approach zero, and the function $R_{i'ik}$ becomes invariant to shifts in those μ 's. This emphasizes the need for strategic positioning of the complementary sources to minimize the effect of changes in μ in iterative image reconstruction. Therefore, the effect of the linear scattering term is greatly reduced in favor of the competing exponential term of the attenuation of the incident radiation, causing the latter to be the main driving force in the image reconstruction process. Solving for $\overrightarrow{\mu}$ is less ambiguous, since it does not depend on direction (unlike $\overleftarrow{\mu}$), because $\overrightarrow{\mu}$ is a function of the source energy and not a function of direction. In addition, given that, at the same photon energy for the same material, $\overrightarrow{\mu} \leq \mu$ (total cross section is always less than or equal that of Compton scattering) and $\overrightarrow{\mu} < \overleftarrow{\mu}$ (cross section at the incident energy is always less than that at the lower photon scattering energy), solving for $\overrightarrow{\mu}$ makes the problem less susceptible to attenuation.

It should be noted that at a given voxel l in the path of an incoming elementary beam j , only one of the partial derivatives of (10) or (11) usually exists, since an elementary beam can either belong to source i' or source i , but not to both simultaneously. The exception to this rule is when a voxel lies at the intersection of two elementary beams emerging from paired sources. At the voxel of intersection, both the partial derivatives of (10) or (11) exist, but have opposite signs as a result of the definition of R in (6). The two derivatives will then tend to cancel each other at the voxel of intersection, in a manner not unlike that of the partial derivatives (8) and (9). As a consequence, the voxels at the intersection of elementary source beams are insensitive to variation in their $\overrightarrow{\mu}$ values. Therefore, we excluded these voxels of intersection from the image reconstruction problem. Fortunately, the sources can be arranged so that these voxels of intersection occur at the deep end of the imaging domain. Therefore, at the deepest row of each imaging domain, predetermined $\overrightarrow{\mu}$ values were assigned, and remained constant throughout the solution process. Alternatively, one can impose a fictitious but known material at the deepest voxel row to achieve the same effect.

E. Analysis

Although the function $R_{i'ik}$ behaves much differently than $S_{i'k}$ and S_{ik} , it can be stated that a solution, $\overrightarrow{\mu}$, to the objective function of absolute measurements, (4), is also a solution for (5), since $R_{i'ik}$ is simply a ratio of the S values. However, the opposite is not true, that is if another solution exists to a system based on (5), it may not be identical to the solution for the corresponding system based on (4). Let us assume that an alternative solution $\overrightarrow{\mu} + \mathbf{b}$ exists, that is a solution shifted by some vector

\vec{b} , then both solutions must produce the same values for R . This requires, based on (6), that

$$\begin{aligned}
& \frac{1}{S_{i'k}^*} \sum_{j=1}^J c_{i'jk} \exp \left[- \sum_{l=1}^{L_{i'jk}} (\vec{\mu}_{i'jl} + b_{i'jl}) x_{i'jl} \right] \\
& \times \mu_{i'jk} \exp \left[- \sum_{n=1}^{N_{i'jk}} \overleftarrow{\mu}_{kn} y_{kn} \right] \\
& - \frac{1}{S_{ik}^*} \sum_{j=1}^J c_{ijk} \exp \left[- \sum_{l=1}^{L_{ijk}} (\vec{\mu}_{ijl} + b_{ijl}) x_{ijl} \right] \\
& \times \mu_{ijk} \exp \left[- \sum_{n=1}^{N_{ijk}} \overleftarrow{\mu}_{kn} y_{kn} \right] \\
& = \frac{1}{S_{i'k}^*} \sum_{j=1}^J c_{i'jk} \exp \left[- \sum_{l=1}^{L_{i'jk}} \vec{\mu}_{i'jl} x_{i'jl} \right] \\
& \times \mu_{i'jk} \exp \left[- \sum_{n=1}^{N_{i'jk}} \overleftarrow{\mu}_{kn} y_{kn} \right] \\
& - \frac{1}{S_{ik}^*} \sum_{j=1}^J c_{ijk} \exp \left[- \sum_{l=1}^{L_{ijk}} \vec{\mu}_{ijl} x_{ijl} \right] \\
& \times \mu_{ijk} \exp \left[- \sum_{n=1}^{N_{ijk}} \overleftarrow{\mu}_{kn} y_{kn} \right] \quad (12)
\end{aligned}$$

where the b values represent shifts in the elements of the vector $\vec{\mu}$. This is obviously a very restrictive condition that must be satisfied at every complementary pair of beams and the corresponding detector. Even when considering the approximate $R_{i'ik}$ value of (7), the condition for two solutions requires

$$\begin{aligned}
& \frac{1}{S_{i'k}^*} \exp[-(\vec{\mu}_{i'k} + \tilde{b}_{i'k}) \vec{X}_{i'k}] \\
& - \frac{1}{S_{ik}^*} \exp[-(\vec{\mu}_{ik} + \tilde{b}_{ik}) \vec{X}_{ik}] \\
& = \frac{1}{S_{i'k}^*} \exp[-\tilde{\mu}_{i'k} \vec{X}_{i'k}] - \frac{1}{S_{ik}^*} \exp[\tilde{\mu}_{ik} \vec{X}_{ik}] \quad (13)
\end{aligned}$$

with the \tilde{b} 's representing average values along each beam, which is satisfied when $\tilde{b}_{i'k} = \tilde{b}_{ik} = 0$ (a trivial case), or when the imaged object is uniform and all source pairs are symmetric and produce exactly the same measured detector response (so that the equality in (13) with both sides being equal to zero is satisfied). A similar argument can be made for two solutions that differ from each other by a scaling factor, which in the case of the approximate condition of (7) requires identical scaling factors for each value of $\vec{\mu}$, or the same uniform symmetric conditions as above. Therefore, one can state that the conditions for obtaining more than one solution for the objective function of relative measurements, (5), are quite restrictive. As such, if a solution exists, it is very likely to be unique; otherwise the iterative process may not converge.

III. ALGORITHM AND NORMS

A. Image Reconstruction

Image reconstruction proceeds progressively from one approximation to another using the Jacobian-driven Newton-Raphson's approach. That is, a solution is found for $\Delta \vec{\mu}$, the vector difference between two successive approximations. We assumed here that $\vec{\mu}$, μ and $\overleftarrow{\mu}$ are interlaced, i.e., once $\overleftarrow{\mu}$ is known (or guessed), the other two vectors are automatically determined (either via the assumption of Compton scattering dominance or via predetermined relationships).

We solve the matrix equation

$$R = D \Delta \vec{\mu} \quad (14)$$

where the elements of vector R are the $\{(S_{i'k})/(S_{ik}^*) - (S_{ik})/(S_{ik}^*)\}$ values and D is the Jacobian matrix, in which an element D_{ml} is given by

$$D_{ml} = -\frac{\partial}{\partial \vec{\mu}_l} \left(\frac{S_{i'k}}{S_{i'k}^*} - \frac{S_{ik}}{S_{ik}^*} \right) \quad (15)$$

where m defines a particular pair of sources, (i', i) , contributing to a certain detector, k . In essence, the formulation of (14) attempts to balance the relative error between calculated (forward modeled) and input (measured) detector responses.

When inverting (14), a smoothing regularization [14] constraint is added to assist the image reconstruction process, since physical objects are usually smooth, at least within certain regions. This is a typical constraint in image processing, where a voxel tends to be similar to that of its neighboring voxels. The successive approximation solution at iteration ℓ then becomes

$$\vec{\mu}_{\ell+1} = [D^T W D + \gamma G]^{-1} D^T W [R + D \vec{\mu}_\ell] \quad (16)$$

where W is a diagonal weighting function, with each element corresponding to the weight given to each ratio of detector responses, γ is a regularization parameter, and G is a matrix that relates each voxel to adjacent neighbors and is structured so that the difference between the attenuation coefficient of a voxel and that of its closest neighbors is minimized; see [11] for details.

A lower bound was imposed on the solution so that non-positive values were set to zero, since they are not physically allowed, and can skew the iterative process considerably due to the exponential nature of the forward mapping, (1). In addition, an upper bound for the value of $\vec{\mu}$, called here $\vec{\mu}_{\max}$, was set at a value of 0.9 cm^{-1} so that the exponential term in the forward model does not become insignificant (has a close to zero value). This upper limit is equal to about four times the attenuation coefficient in water for a 102 keV X-ray source. The upper limit ensures that measurements are not so weak that they are insensitive to changes in $\vec{\mu}$.

B. Image Quality Factors

The above proposed image reconstruction method was tested numerically in a number of situations. The quality of the reconstructed images was assessed using the factors described below.

Since the method solves for relative measurements, rather than absolute values, two types of error factors were introduced here: one that reflects global changes in magnitude and the other measures localized discrepancies adjusted for magnitude error. However, the first factor examined directly the behavior of the objective function.

1 *Residual* (δ_R)

$$\delta_R = \frac{1}{N_R} \| \mathbf{R} - \mathbf{D} \Delta \vec{\mu} \| \quad (17)$$

where $\| \cdot \|$ designates the Euclidean norm and N_R is the number of measurement ratios used in the calculations (i.e., the number of available equations). This factor estimates how close the calculated ratios are to the analogous ones obtained from the measurements.

2 *Measurement scaling factor* (c_S)

$$c_S = \frac{\sum_{i=1}^{N_S} S_i^*}{\sum_{i=1}^{N_S} S_i} \quad (18)$$

where N_S is the number of measurements. This factor determines the overall (global) matching between the magnitudes of the input and calculated detector responses.

3 *Measurement error* (δ_S)

$$\delta_S = \sqrt{\frac{\sum_{i=1}^{N_S} (c_S S_i - S_i^*)^2}{\sum_{i=1}^{N_S} (S_i^*)^2}}. \quad (19)$$

This factor measures the matching between scaled calculated detector responses and the input values. The scaling of the calculated detector responses is introduced here so that the factor reflects localized discrepancies, free from the influence of the overall estimated signal magnitude.

4 *Image scaling factor* (c_μ)

$$c_\mu = \frac{\sum_{i=1}^{N_\mu} \vec{\mu}_i^*}{\sum_{i=1}^{N_\mu} \vec{\mu}_i} \quad (20)$$

where N_μ is the number of voxels. Analogous to c_S , this factor determines how the global magnitude of the reconstructed $\vec{\mu}$ values matches that of the actual image (assumed to be known in advance in this work, in order to test the algorithm).

5 *Image error* (δ_μ)

$$\delta_\mu = \sqrt{\frac{\sum_{i=1}^{N_\mu} (c_\mu \vec{\mu}_i - \vec{\mu}_i^*)^2}{\sum_{i=1}^{N_\mu} (\vec{\mu}_i^*)^2}}. \quad (21)$$

This factor measures the localized (voxel-by-voxel) changes between scaled reconstructed values of $\vec{\mu}$ and the actual values.

In order to streamline data presentation certain factors will be presented together as a transposed vector:

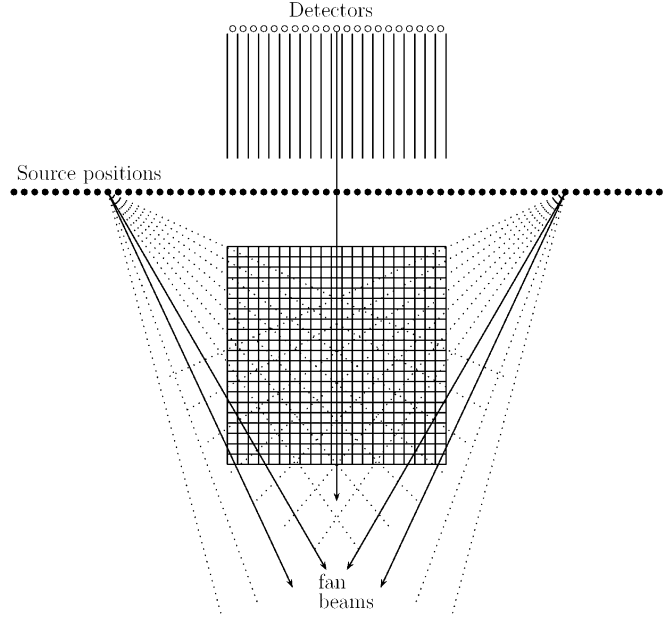


Fig. 3. Single-side scanner layout. Solid circles represent the source's position increments while it translates across the subject and empty circles represent detectors. Solid arrows show an active pair of sweeping source fan beams, while dotted lines indicate increments or source beams as they sweep across the object.

$\{N, \delta_R, c_S, \delta_S, c_\mu, \delta_\mu\}$, where N is the number of iterations at which the factors are reported. In all cases, the solution starts with a guess of a uniform distribution of the attenuation coefficient across the imaged object. Our results showed that the solution was not sensitive to the value used for the initial guess, whether low or high.

IV. EXAMPLE FOR ONE-SIDE TOMOGRAPHY

One of the main attractive features of scatter imaging is the ability to image objects that are not accessible from both sides, by exposing the object and acquiring the measurements from one side. Example applications include the imaging of pressure vessels while in service, examining aircraft and concrete structures, and inspecting a suspicious package left near a wall.

A. Setup

The one-side imaging capability was demonstrated on a section extending from the surface to 210 mm deep, with a width of 210 mm. The section was divided into 21×21 equal cubic voxels (1 cm^3 each), as shown in Fig. 3, and was given a uniform attenuation coefficient of $\vec{\mu} = 0.2 \text{ cm}^{-1}$ (a value comparable to that for water at the employed source energy), except for some void areas ($\vec{\mu} = 0 \text{ cm}^{-1}$) and dense regions ($\vec{\mu} = 0.35 \text{ cm}^{-1}$). Note that the thickness of the object in the part free of inclusions is equal to 4 mfp, which far exceeds the 1 mfp normally used for scatter-only (without transmission) measurements [5], [6]. Scatter imaging was assumed to be acquired using a fan beam moving along a line parallel to the exposed surface at the level of the plane at which a tomographic two-dimensional (2-D) image is to be reconstructed. The source, placed 52.5 mm away from the surface of the imaged section, stopped at voxel-width increments to sweep a 5° fan beam across the section. Only the re-

sponse of source beams intersecting with voxels were recorded. An array of collimated detectors, placed 210 mm away from the surface, were aligned along another line parallel to the source line and at the same level. These detectors record scattered radiation (protected from direct source exposure), with each detector viewing a column of image voxels along the depth of the section. A total of 3599 detector responses were available for 420 unknown attenuation coefficient (voxels), leading to an overdetermination of the problem by a factor of 8.6. This high degree of overdetermination is another unique feature of scatter imaging, where more than one measurement can be recorded for the same source (unlike in transmission techniques where only measurements downstream of the incident radiation are useful).

B. Ideal Problem

First, a test with ideal input detector responses (error-free measurements calculated using the forward model) was performed in order to ensure that the computer program implementing the imaging process was functioning as intended. With error-free “measurements”, the exact (actual) image should be reconstructed. The results of this exercise, reported in detail in [11], showed that the successive approximation process converges, in about six iterations. The process was continued however to 20 iterations to ensure that it is not susceptible to error propagation. An image quality vector of $\{N = 20, \delta_R = 1.245 \times 10^{-8}, c_S = 1.000, \delta_S = 1.047 \times 10^{-5}, c_\mu = 1.000, \delta_\mu = 1.955 \times 10^{-5}\}$ was obtained, indicating almost negligible discrepancy between the measurements and the calculated detector responses. This nearly perfect image reconstruction is shown in Fig. 4. Note though there was no need for regularization since the problem was error-free.

C. Inversion With Disturbed Detector Responses

The real test of an image reconstruction process is in its ability to accommodate any discrepancies between measurements \mathbf{S}^* and the detector responses calculated by the forward model, \mathbf{S} . Such discrepancies arise, not only because of the idealization of the forward model, but also can be introduced by systematic (calibration and setup) errors and random counting uncertainties. In order to study these discrepancies, the \mathbf{S} values were disturbed by adding white noise, sampled from a normal distribution with a relative (to the mean) standard deviation of 12%. This high level of disturbance was considered more than sufficient to account for statistical variations, effects of idealization in modeling the problem, fluctuations in source emission rate, etc. Although the common practice is to reduce the contribution of measurements with large uncertainty by giving them a lower weight, via matrix \mathbf{W} in (16), we used a value of \mathbf{W} equal to the identity matrix in order to avoid further damping of the weaker contributions of deep voxels.

Regularization is required to bound and guide the solution process. When attempting to reconstruct an image without regularization, the behavior of the iterative process was erratic as one would expect, and the reconstructed image was quite noisy, with no identifiable image features. However, a small amount of regularization stabilized the problem considerably, as evident

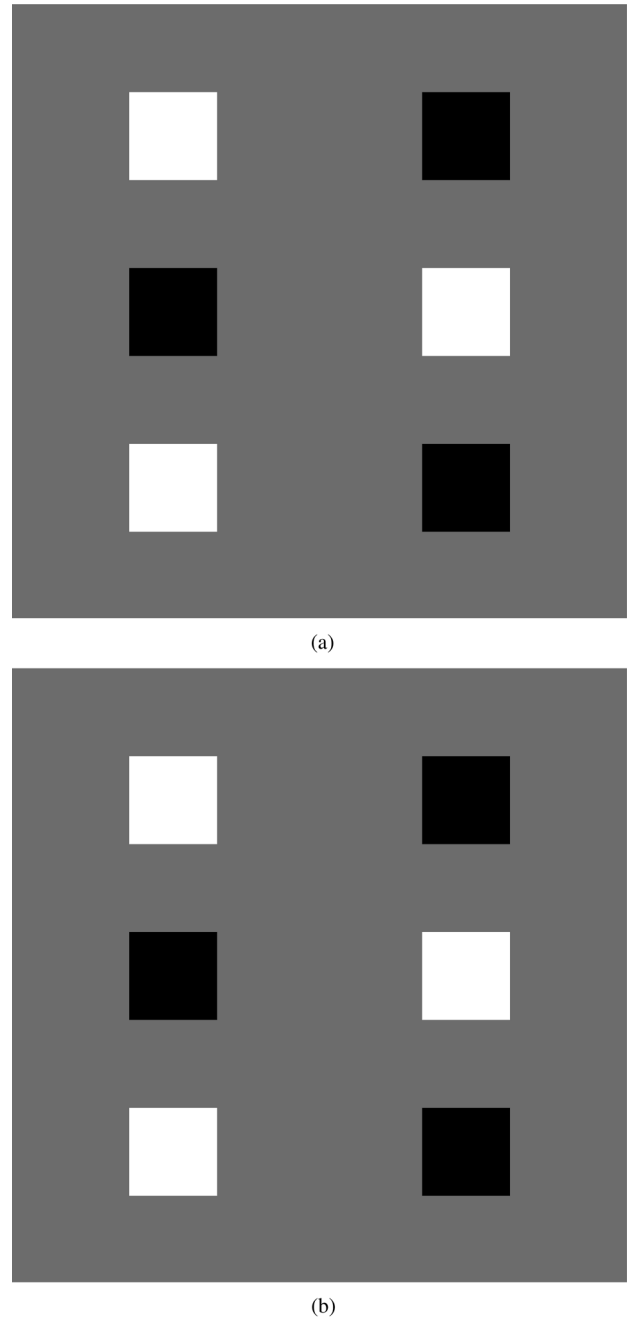


Fig. 4. Reconstructed image after 20 iterations using ideal measurements (without regularization). (a) Actual image. (b) Reconstructed image using ideal forward measurements.

TABLE I
CHANGE IN CONDITION NUMBER OF INVERTED MATRIX (AFTER 10 ITERATIONS) IN THE PRESENCE OF 12% DISTURBANCE IN DETECTOR RESPONSE

γ	0.0	0.5	2.5	4.0
Condition Number	95921	140	154	160

by the significant decrease in the condition number of the inverted matrix, shown in Table I, for different values of the regularization parameter γ of (16) after 10 iterations. The condition number in this table is reported after a fixed number of iterations to enable consistent comparability, since the nonlinear nature of the problem can cause the condition number to vary

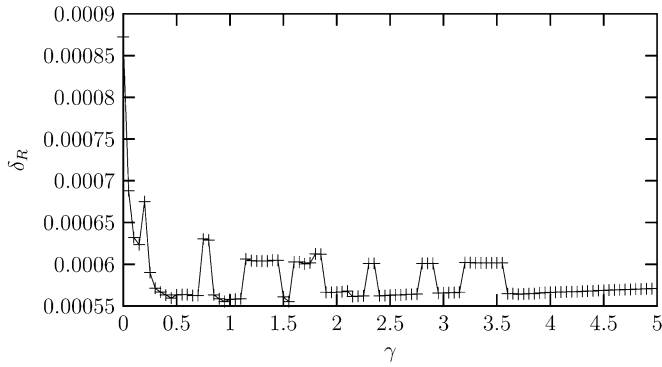


Fig. 5. Residual (δ_R) for various regularization levels (γ values) after 10 iterations, with detector response disturbed by a 12% random noise.

during the iterative process. It should be noted that a γ value of about 30 makes the smoothing matrix \mathbf{G} in (16) have about the same amount of influence on the solution as the system response matrix $\mathbf{D}^T \mathbf{W} \mathbf{D}$. Therefore, even the highest value of γ reported in Table I was still reasonably mild. The drastic stabilization with a small value of γ was attributed to the role regularization plays in imposing order on the problem. Without regularization, the first estimate of $\vec{\mu}$ would be quite drastically different from the actual solution. Since the Jacobian matrix \mathbf{D} , of (15), is constructed based on the value of $\vec{\mu}$ in the previous iteration, the matrix \mathbf{D} will be also affected by the noise. This effect will be propagated through from one iteration to another, leading the solution astray, as reflected by the very high condition number recorded in Table I. In essence, the error overwhelms the problem and destroys any orderly behavior, or consistency, that should have been provided by the many available measurements. Adding a small amount of regularization restores order, as evident by the drastic change in the conditioning number obtained for $\gamma = 0.5$ in Table I, since each voxel in the image is forced to relate to its neighbors. Additional regularization would lead to further smoothness of the image, without severely affecting the structure of the system response matrix.

The effect of regularization was demonstrated by observing the change of the residual, δ_R , with the regularization parameter γ , shown in Fig. 5. Fig. 5 indicates that a small amount of regularization stabilizes the problem significantly, as shown by the sharp drop in δ_R . However, as the value of γ increased, δ_R began to exhibit an oscillatory behavior. Changing the number of iterations did not affect the general features of the trend, except by shifting the position of the oscillations observed at the medium values of γ . The oscillation of δ_R is due to the nature of the iterative process, which is constrained by the imposition of upper and lower bounds on the solution. The more restrictive these constraints, the more the iterative process tries to restore the unconstrained features, and so on. We have confirmed this by plotting the amount of clipping (exceeding the solution bounds), which also exhibited the same oscillatory behavior particularly in case of the non-negative constraint. At large values of γ , this behavior of δ_R stabilizes because of the dominance of regularization, which reduces the amount of corrective action imposed by solution bounding.

In order to avoid excessive smoothing that can conceal the image features, while staying away from the oscillatory

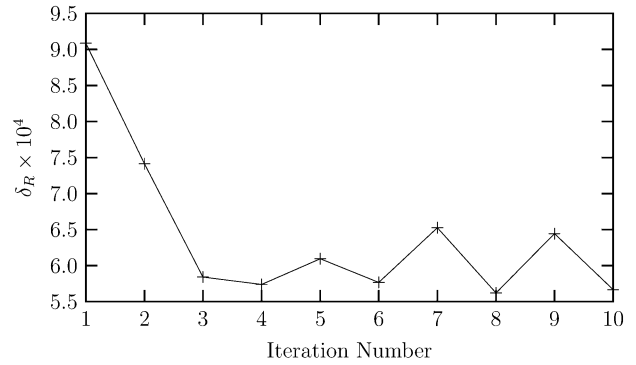


Fig. 6. Residual (δ_R) during image reconstruction using $\gamma = 0.5$ for detector response disturbed by a 12% random noise.

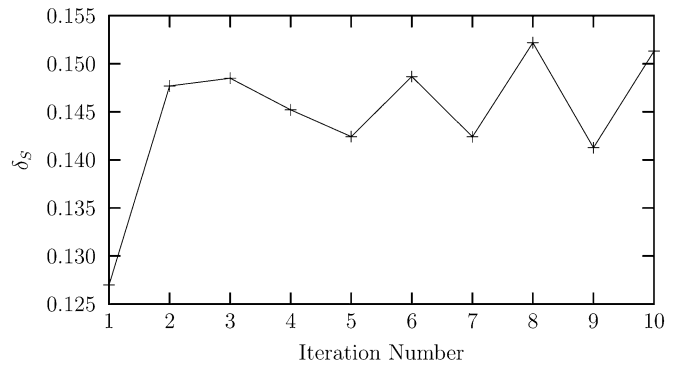


Fig. 7. Measurement error (δ_S) during image reconstruction using $\gamma = 0.5$ for detector response disturbed by a 12% random noise.

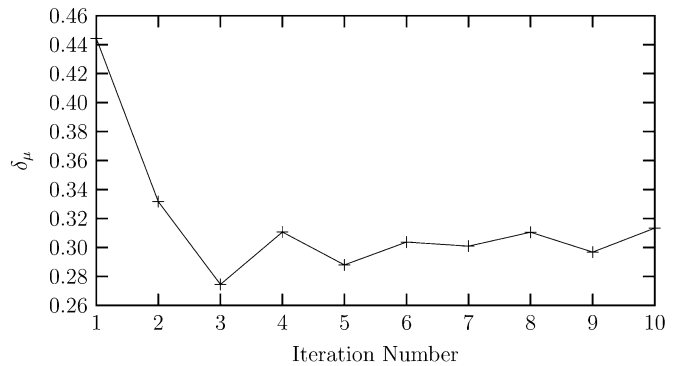


Fig. 8. Image error (δ_μ) during image reconstruction using $\gamma = 0.5$ for detector response disturbed by a 12% random noise.

behavior of δ_R , we have decided to utilize a small value of γ . We selected $\gamma = 0.5$ at the tail end of the steep drop in δ_R observed in Fig. 5. The image quality factors, δ_R , δ_S , and δ_μ , for this value of γ are plotted in Figs. 6–8, respectively. All the quality factors tended to converge, albeit with some oscillatory behavior. These oscillations were attributed to the imposition of a lower (non-negative) bound on the solution as discussed above. The value of δ_S did not exceed 0.155, a rather good value given the input value at 0.12. The image error, δ_μ , appeared to settle at a value of about 0.32, in spite of the reasonably low value of the residual error $\delta_R \approx 6 \times 10^{-4}$. It is interesting to notice that δ_R and δ_μ exhibit a similar trend, while δ_S behaves differently. This is expected since the problem is solved for

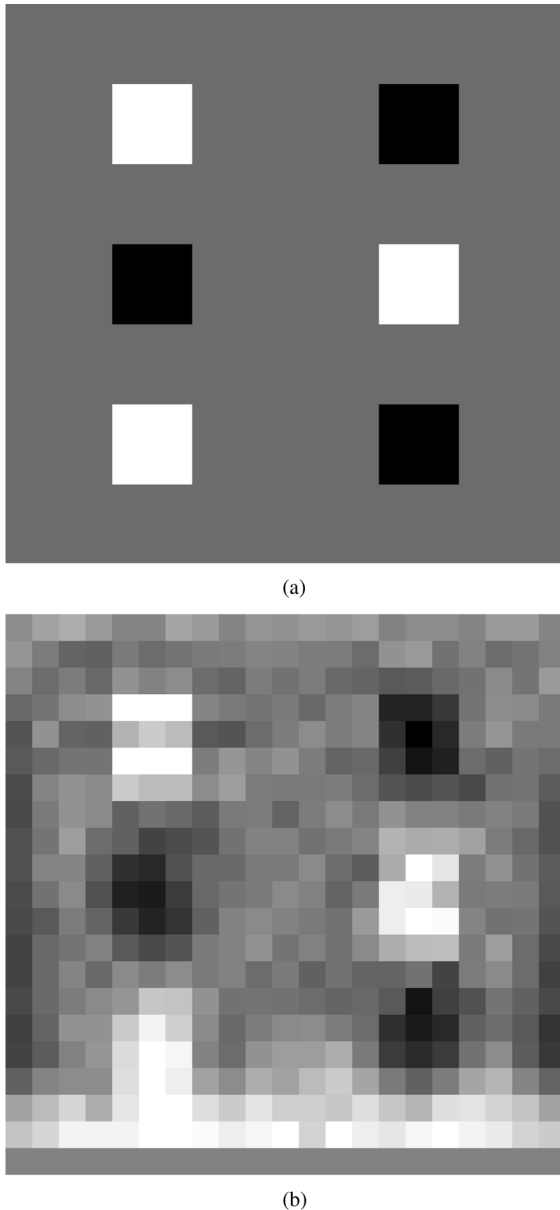


Fig. 9. Reconstructed image after 10 iterations using $\gamma = 0.5$. (a) Actual image. (b) Reconstructed image using disturbed forward measurements.

best matching with the measurement ratios, while δ_S measures the matching of absolute measurements. The residual error, δ_R , provides a better reflection of the solution behavior, i.e., best matching with measurements ratios. However, in spite of the low value of δ_R , the image error, δ_μ , was still quite high, reflecting the high level of disturbance in detector response. Nevertheless, all the original image features were captured in the reconstructed image, as shown in Fig. 9. An image quality vector of $\{N = 10, \delta_R = 5.6655 \times 10^{-4}, c_S = 1.0422, \delta_S = 0.1513, c_\mu = 1.0091, \delta_\mu = 0.3133\}$ was obtained. The proximity of c_S and c_μ to unity indicates that the ratios between the calculated and known values are nearly identical, which is indicative that the reconstruction process maintained the general distribution trend for both \mathcal{S} and $\vec{\mu}$. Therefore, in spite of this excessively high degree of error, the reconstruction

algorithm was remarkably able to retrieve the image features, as it relies on relative measurements rather than absolute ones.

D. Summary

The results above show that the introduced scheme is quite robust, as it converges smoothly to an acceptable solution (in spite of some initial instability in matching calculated detector responses with input values). For error-free (ideal) detector responses, the inversion was nearly perfect. Even with highly disturbed detector responses, a reasonable image was obtained. This image reconstruction was possible up to a depth of about 4 mfp in a thick object, and without the need for supplementary transmission measurements as was done in the past. This shows that pure one-side imaging in a relatively thick object is attainable.

V. EXAMPLE FOR A MULTILAYERED STRUCTURE

One of the main attractive features of scatter imaging is that it can benefit from measurements that can be recorded anywhere in the three-dimensional space. Three-dimensional measurements enrich the scatter imaging process, as it enables the acquisition of off-plane measurements. We examine here the three-dimensional (3-D) single-side imaging of a test object and compare it to the 2-D (slice-by-slice) imaging of the same object, to demonstrate the merit of 3-D scatter imaging. We also take advantage of this setup to examine the effect of the degree of overdetermination on image quality.

Image reconstruction in 3-D was achieved by stacking grids of the above 2-D problem, referred to here as the x - y problem, to form a volume. Each x - y slice was then exposed to radiation, with fan-beam sources in a manner similar to that of Fig. 3. The source-detector assembly was then moved one voxel level in the z direction, and another set of measurements were acquired for the adjacent x - y grid of voxels. This procedure was then repeated for the rest of the volume. With the volume being rastered once, the entire process is repeated for the same volume but using z - y instead of x - y slices. This doubles the number of independent measurements. Note that with the proper scanner layout it is physically possible to conduct measurements in the x - y and z - y planes simultaneously. Although, it is possible to acquire many more measurements at each exposure, this was not done to avoid further complication of the calculations. The setup was further simplified by widening the fan beam angle to 10° , instead of 5° as in the previous example problem, and by fixing the beam orientation into two specific fan beams orientations at 45° and its mirror image, as illustrated in Figs. 10 and 11. An image was reconstructed only to a depth of 6 voxels (providing a depth of 1.3 mfp), to produce an image within $21 \times 21 \times 6$ voxels. For simplicity, the reconstructed phantom consisted of uniform layers, so that all x - y and z - y slices are identical, but with varying values of $\vec{\mu}$, as shown in Fig. 15(a). After confirming that near perfect image reconstruction was possible with error-free detector responses, to ensure that the inversion algorithm was correctly programmed, the ideal data were disturbed only by 2% noise. A low noise level was employed here since the main interest was to compare 3-D measurements to those of 2-D. This level of disturbance was chosen to be sufficiently large to influence the reconstructed image, but small enough that

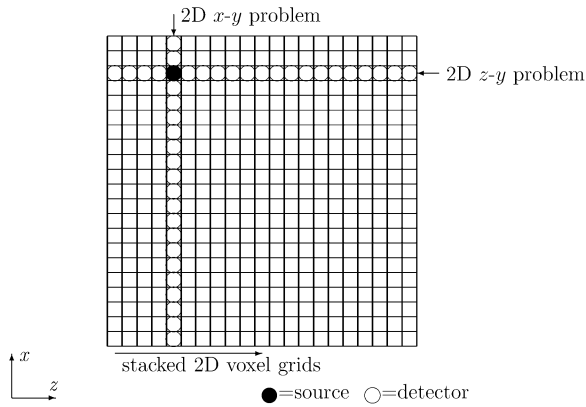


Fig. 10. Top view of the 3-D scanner layout (x - z plane), showing a single source position and corresponding detectors. The source and detectors are aimed into the page. A 3-D block is constructed by stacking voxel grids of Fig. 3. The source is placed where linear detector arrays cross.

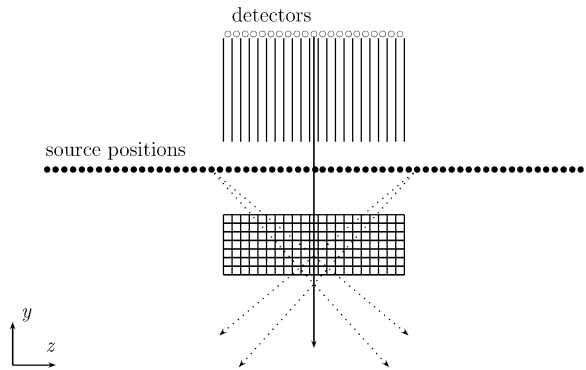


Fig. 11. Side view (x - y or z - y plane) of the 3-D scanner layout. Solid circles represent source increments and empty circles represent detectors. The dotted lines illustrate the source fan beam.

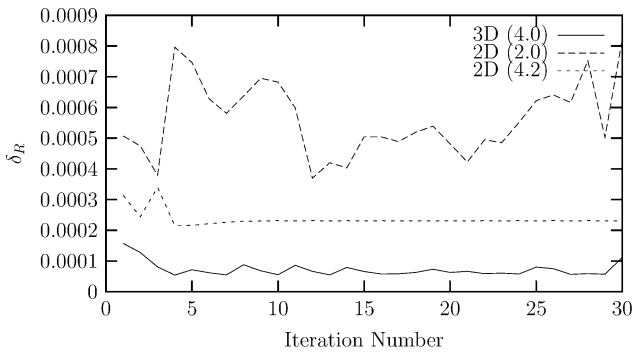


Fig. 12. Residual (δ_R) during image reconstruction for 3-D and 2-D imaging (without regularization), where the number in parentheses indicates the degree of overdetermination.

image reconstruction can be performed without regularization. The objective here is to explore the 3-D imaging potential of the problem, without being entangled with numerical problems the nature of which were investigated in the 2-D problem in Section IV.

In the problem described above, one reconstructs two identical 2-D images, one in x - y and the other in z - y . Either 2-D problems are now overdetermined by a factor of

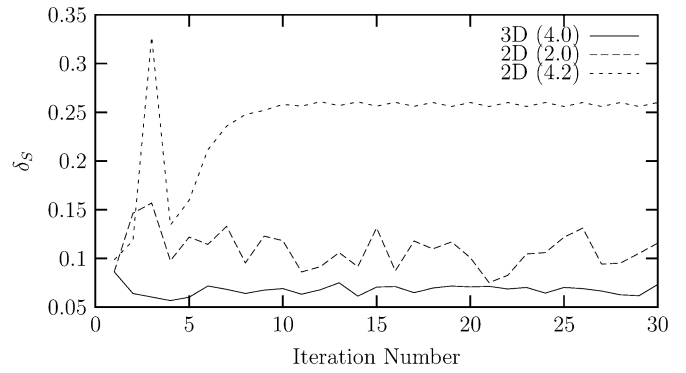


Fig. 13. Measurement error (δ_S) during image reconstruction for 2-D (2.0), 2-D (4.2), and 3-D (4.0) imaging (without regularization), where the number in parentheses indicates the degree of overdetermination.

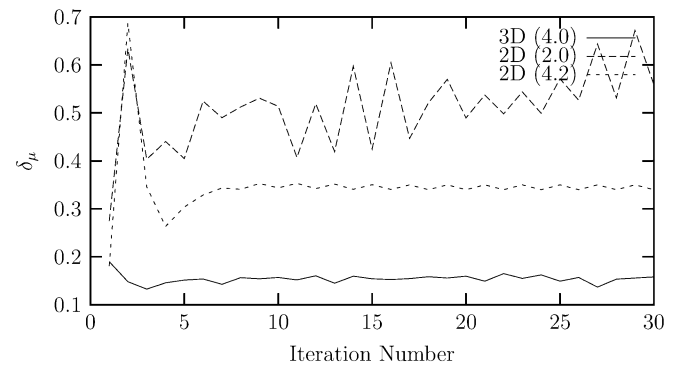


Fig. 14. Image error (δ_μ) during image reconstruction for 3-D and 2-D imaging (without regularization).

2.0 (compared to 8.6 in the previous example). The reconstructed images resulted in the image quality vector: $\{N = 30, \delta_R = 8.2130 \times 10^{-4}, c_S = 1.014, \delta_S = 0.1159, c_\mu = 0.9413, \delta_\mu = 0.5592\}$. As Fig. 13 shows, the iterative process tended to diverge during the 30 iterations considered. Accordingly, the measurement error behaved erratically as shown in Fig. 13, while the image error was quite high and got worse as the number of iterations increased (Fig. 14). Therefore, the reconstructed image shown in Fig. 15(b) was quite poor. Interestingly though, the values for δ_S were lower than those obtained in the other 2-D case discussed below, where convergence was attained. These lower values were due to the fact that this case lent itself to producing measurements that are alike in magnitude, due to the use of relatively wide source beams and the confinement of the measurements to one section. Nevertheless, this shows that the problem in the presence of noise is susceptible to divergence if the problem is not highly overdetermined and is not subjected to regularization. Note that error-free problems produced good images for the same setup.

In order to demonstrate that the divergence of the above problem was due to the relatively small number of available measurements, a second set of measurements was generated so that the 2-D problem was overdetermined by a factor of 4.2. The additional degree of overdetermination was achieved by subdividing the source beam into three narrower fan beams, providing a greater number of measurements. The image quality vector for

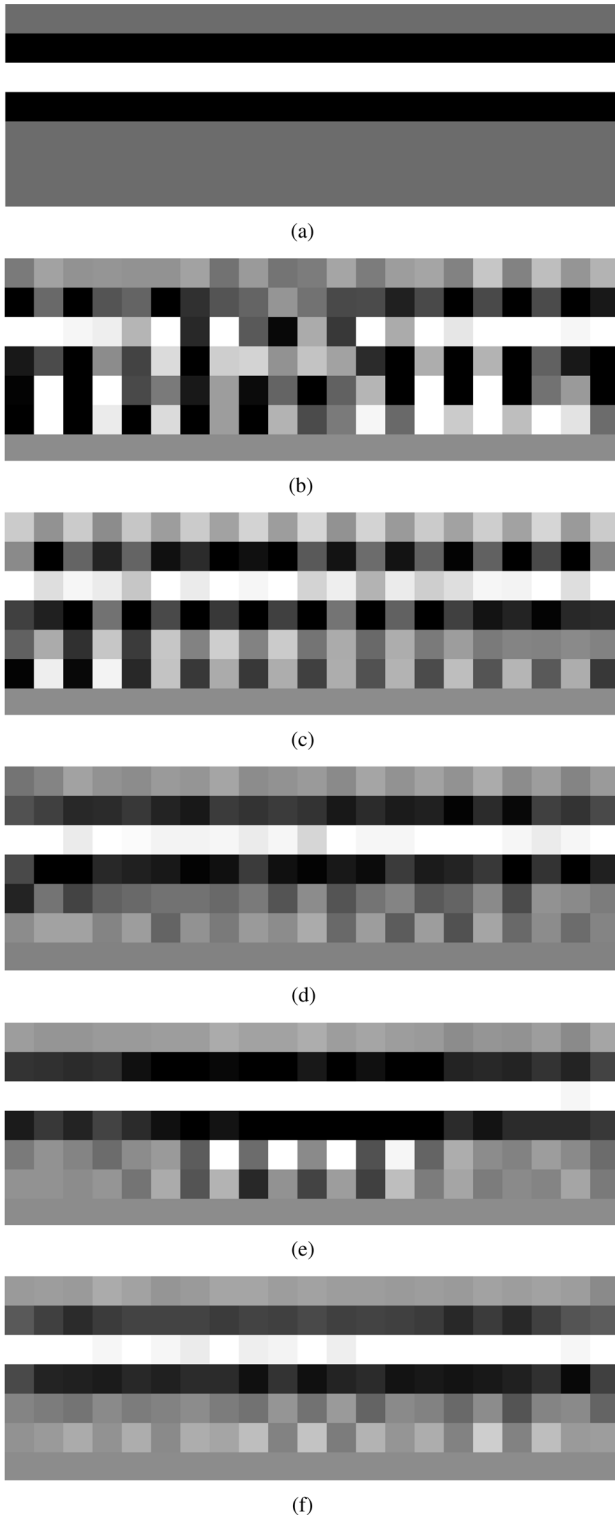


Fig. 15. Images reconstructed by 3-D scatter imaging using disturbed measurements, where the number in parentheses indicates the degree of overdetermination. (a) Actual image: 3 layers in x - y or z - y with uniform x - z layers of $\vec{\mu}$ equal to either 0, 0.2 or 0.35. (b) Two-dimensional reconstructed image (2.0). (c) Two-dimensional reconstructed image (4.2). (d) 3-D reconstructed image (4.0): first slice. (e) Three-dimensional reconstructed image (4.0): tenth slice. (f) Three-dimensional reconstructed image (4.0): 21st slice.

the more overdetermined 2-D image reconstruction using disturbed measurements is $\{N = 30, \delta_R = 2.3120 \times 10^{-4}, c_S = 1.082, \delta_S = 0.2600, c_\mu = 0.9666, \delta_\mu = 0.3401\}$. All quality

factors stabilized once the problem converged, as shown in Figs. 12–14. The reconstructed image, shown in Fig. 15(c), though not yet perfect, was better than the previous case. However, both the measurement and the image errors were quite high, due to the use of a finer beam which tended to produce measurements that can vary widely in magnitude from each other, since they are affected by a small number of voxels that can be quite far apart and different in content from each other. The low residual error indicates that the method, by depending on ratio of measurements, can reproduce the general features of a structure.

The 3-D problem is overdetermined by a factor of 4.0, since two orthogonal sets of measurements are available for this layout. This is a level of overdetermination that is comparable to that of the above 2-D problem. However, a much better image quality vector was attained for 3-D imaging: $\{N = 30, \delta_R = 1.1156 \times 10^{-4}, c_S = 1.030, \delta_S = 0.07331, c_\mu = 0.9881, \delta_\mu = 0.1581\}$. The images obtained at various slices were also much improved, as shown in Fig. 15. The problem converged nicely and rapidly for all quality factors, see Figs. 12–14. Since the degree of overdetermination of the 3-D reconstruction was about equal to the above 2-D reconstruction, for same source and detector setup, there is obviously a mitigating effect that improves the 3-D problems considerably. We attribute this improvement to the increased contrast provided by the off-plane measurements, as radiation has to cross various paths which are quite different in length. In essence, overdetermination provides additional constraints to the solution of the problem, and the constraints imposed by 3-D measurements are more restrictive than those in a 2-D configuration.

VI. SUMMARY AND CONCLUSION

This paper showed that by iteratively solving the inverse problem of radiation scatter imaging to minimize the residuals of the ratio of measurements with overlapping fields of view, and solving for the attenuation coefficient of the non-overlapping voxels, both 2-D and 3-D images of relatively thick/dense objects can be reconstructed. The method was numerically tested for the single side imaging of an object about four mean-free-paths deep in the presence of measurements disturbed by 12% random noise. With a degree of overdetermination of 8.6, and with the aid of regularization, reasonably good images were reconstructed after a few iterations. In the side scatter imaging of a 3-D object, it was demonstrated that 2-D tomographic imaging of various orthogonal sections is not as successful as the simultaneous 3-D reconstruction of the object, even when the degree of overdetermination was increased for section imaging. This not only demonstrates that scatter imaging lends itself naturally to 3-D imaging, but also that 3-D measurements add rich (more distinct and independent) measurements that enhance the image reconstruction process. The full potential of 3-D scatter imaging is yet to be fully explored. In spite of the relativism of the transformed inverse problem (i.e., its reliance on measurement ratios, rather than absolute measurements), the reconstructed images had correct (not relative) values. This is likely due to the extra complexity provided by fan-beam sources, which constrain the system

so that a reconstructed image must have the correct absolute values in order to reproduce the utilized relative measurements.

An important compromise that was necessary to attain a solution was that the deepest set of voxels of the image were assumed to be known. Although deepest voxels act as reference points and can be fictitiously assigned, future work will aim at finding better ways to overcome this problem, as well as introducing a smoother approach to solution bounding. The practical challenges of this imaging scheme are currently being investigated. Nevertheless, this work is an essential step in tackling the nonlinearity of the problem and enabling it to go beyond previous restrictions, while allowing the use of scatter imaging without the aid of supplementary transmission measurements.

ACKNOWLEDGMENT

This work was inspired by efforts to develop scatter-imaging systems funded by the U.S. Federal Aviation Administration under Grant Number 97-G-029.

REFERENCES

- [1] P. G. Lale, "The examination of internal tissues, using gamma-ray scatter with a possible extension to megavoltage radiography," *Phys. Med. Biol.*, vol. 4, pp. 159–167, 1959.
- [2] F. T. Farmer and M. P. Collins, "A new approach to the determination of anatomical cross-sections of the body by Compton scattering of gamma-rays," *Phys. Med. Biol.*, vol. 16, pp. 577–586, 1971.
- [3] J. J. Battista and M. J. Bronskill, "Compton scatter imaging of transverse sections: An overall appraisal and evaluation for radiotherapy planning," *Phys. Med. Biol.*, vol. 26, pp. 81–99, 1981.
- [4] E. M. A. Hussein, D. A. Meneley, and S. Banerjee, "On the solution of the inverse problem of radiation scatter imaging," *Nucl. Sci. Eng.*, vol. 92, pp. 341–349, 1986.
- [5] E. M. A. Hussein, D. A. Meneley, and S. Banerjee, "Single-exposure neutron tomography of two-phase flow," *Int. J. Multiphase Flow*, vol. 12, pp. 1–34, 1986.
- [6] N. V. Arendtsz and E. M. A. Hussein, "Energy-spectral scatter imaging, Part I: Theory and mathematics," *IEEE Trans. Nucl. Sci.*, vol. 42, no. 4, pp. 2155–2165, Apr. 1995.
- [7] T. H. Prettyman, R. P. Gardner, J. C. Russ, and K. Verghese, "A combined transmission and scattering tomographic approach to composition and density imaging," *Appl. Radiat. Isotopes*, vol. 44, pp. 1327–1341, 1993.
- [8] P. Busono and E. M. A. Hussein, "Algorithms for density and composition-discrimination imaging for fourth generation CT systems," *Phys. Med. Biol.*, vol. 44, pp. 1455–1477, 1999.
- [9] F. El Khettabi and E. M. A. Hussein, "An inverse problem for three-dimensional X-ray scatter/transmission imaging," *Inverse Prob.*, vol. 19, pp. 447–495, 2003.
- [10] F. El Khettabi, E. M. A. Hussein, and H. A. Jama, "A nonrotating multi-parameter 3-D X-ray imaging system. Part I: Modeling and reconstruction," *IEEE Trans. Nucl. Sci.*, vol. 51, no. 3, pp. 641–647, Jun. 2004.
- [11] P. A. Arsenaault, "X-ray scatter image reconstruction by balancing of discrepancies between detector responses," Ph.D. thesis, Univ. New Brunswick, Fredericton, AB, Canada, 2004.
- [12] P. J. Arsenaault and E. M. A. Hussein, "X-Ray Scatter Image Reconstruction by Balancing of Discrepancies Between Detector Responses," United States Patent & Trademark Office, Patent Pending, Aug. 2004.
- [13] G. James, *Mathematics Dictionary*, 3rd ed. Princeton, NJ: Van Nostrand, 1968.
- [14] A. N. Tikhonov and V. Y. Arsenin, *Solutions of Ill-Posed Problems*. New York: Winston/Halsted, 1977.